

Twisted phase of the orbital-dominant ferromagnet SmN in a GdN/SmN heterostructureJ. F. McNulty,^{1,*} E.-M. Anton,¹ B. J. Ruck,¹ F. Natali,¹ H. Warring,¹ F. Wilhelm,² A. Rogalev,² M. Medeiros Soares,² N. B. Brookes,² and H. J. Trodahl¹¹*The MacDiarmid Institute for Advanced Materials and Nanotechnology, School of Chemical and Physical Sciences, Victoria University of Wellington, P.O. Box 600, Wellington, New Zealand*²*ESRF-The European Synchrotron, CS40220, F-38043 Grenoble Cedex 9, France*

(Received 25 July 2014; revised manuscript received 10 March 2015; published 22 May 2015)

The strong spin-orbit interaction in the rare-earth elements ensures that even within a ferromagnetic state there is a substantial orbital contribution to the ferromagnetic moment, in contrast to more familiar transition metal systems in which the orbital moment is usually quenched. The orbital-dominant magnetization that is then possible within rare-earth systems facilitates the fabrication of entirely new magnetic heterostructures, and here we report a study of a particularly striking example comprising interfaces between GdN and SmN. Our investigation reveals a twisted magnetization arising from the large spin-only magnetic moment in GdN and the nearly zero, but orbital-dominant, moment of SmN. The unusual twisted phase is driven by (i) the similar ferromagnetic Gd-Gd, Sm-Sm, and Gd-Sm exchange interactions, (ii) a SmN Zeeman interaction 200 times weaker than that of GdN, and (iii) the orbital-dominant SmN magnetic moment. The element specificity of x-ray magnetic circular dichroism is used in separate modes probing both bulk and surface regions, revealing the depth profile of the twisting magnetization.

DOI: [10.1103/PhysRevB.91.174426](https://doi.org/10.1103/PhysRevB.91.174426)

PACS number(s): 75.25.-j, 75.50.Pp

I. INTRODUCTION

An inhomogeneous, twisted magnetic ordering commonly occurs near interfaces between ferromagnetic materials, due to competing interactions that favor opposing alignments of the magnetization. These phases are types of engineered domain walls, and thus have important implications for spintronics applications, where current-driven domain-wall motion is an active area of research [1–4]. So far, twisted phases are known to manifest in diverse magnetic systems [5–12], however these all fall under the conventional spin-dominant paradigm of magnetism where the orbital moment plays no significant role. Competing interactions in the presence of a dominant orbital moment have so far remained unexplored, yet the opportunity now exists within the rare-earth nitride (REN) series, where orbital-dominant magnetism is possible due to strong spin-orbit coupling of the $4f$ electrons. Forming a series of mostly intrinsic ferromagnetic semiconductors [13–19], the RENs are already integrated within spintronic devices [20,21], and thus provide a novel system for studying competing interactions.

The rare-earth elements, comprising the series across which the $4f$ shell is filled, have been of interest for nearly a century. They are most commonly found in the trivalent state in a wide range of compounds, including RENs. The $4f$ shell, with $l = 3$, comprises seven distinct orbital states, $-3 \leq m_l \leq 3$, and with the spin degeneracy a total of 14 single-electron states. Gd^{3+} has a half-filled shell, for which Hund's rules state that the seven electrons fill all of the orbital states with spin-up electrons; $L = 0$ and $S = J = 7/2$. It thus has a purely spin moment of $7\mu_B$. The indirect exchange interaction aligns the spins below a Curie temperature of about 50 K, rising to 70 K under heavy donor doping [22], but the spherical symmetry of the $L = 0$ shell interacts very weakly with the crystalline environment, leading to a coercive field as small as

100 Oe [23]. Sm provides an enormous contrast. In the Sm^{3+} ion there are five electrons in the $4f$ shell, again with full spin alignment ($S = 5/2$) in the Hund's rule ground state, and with an orbital angular momentum $L = 5$ opposing the spin. The simple Hund's rule result is then that the magnetic moment of the $4f$ shell is $\mu = \mu_B \langle L_z + 2S_z \rangle = 0$. As usual, the spin-orbit interaction prevents the multielectron state from adopting fixed m_s and m_l , and the free Sm^{3+} ion has the paramagnetic moment defined by the Landé g factor via $g\sqrt{J(J+1)}\mu_B = 0.84\mu_B$ per ion. In SmN, that is reduced by the crystal field to $0.41\mu_B$, as reported by Meyer *et al.* [24]. However, the net moment in the ferromagnetic state below 27 K is only $0.035\mu_B$ per Sm^{3+} , and it is directed antiparallel to the spin moments that are aligned by interion exchange [24,25]. The orbital moment is then parallel to the net moment, and SmN is properly viewed as an orbital-dominant ferromagnet. The coercive field in SmN is enhanced to over 6 T by the nonspherical $L = 5$ orbital wave function and the very weak Zeeman interaction associated with the small magnetic moment.

Here we exploit the contrasting properties of GdN and SmN in SmN/GdN thin-film heterostructures, and we observe a twisted phase arising from a novel competition between spin and orbital magnetism. The spin-dominant GdN is fixed parallel to an external magnetic field, and its much larger Zeeman interaction ensures that it provides a rigid layer that pins the SmN spin at the SmN-GdN interface. The pinning of the SmN, with its 200-fold weaker Zeeman coupling, takes place through ferromagnetic exchange coupling with the GdN, resulting in a SmN spin moment parallel to that of the GdN, while the orbital moment is antiparallel. This interface pinning is opposed by the orbital-dominant Zeeman alignment of the bulk SmN, which tends to align the SmN magnetization in the opposite sense, and thus drives the rotation of the magnetization across the SmN layer. Figure 1 sketches the effects of exchange coupling between spin and orbital dominant ferromagnets.

*james.f.mcnulty@gmail.com

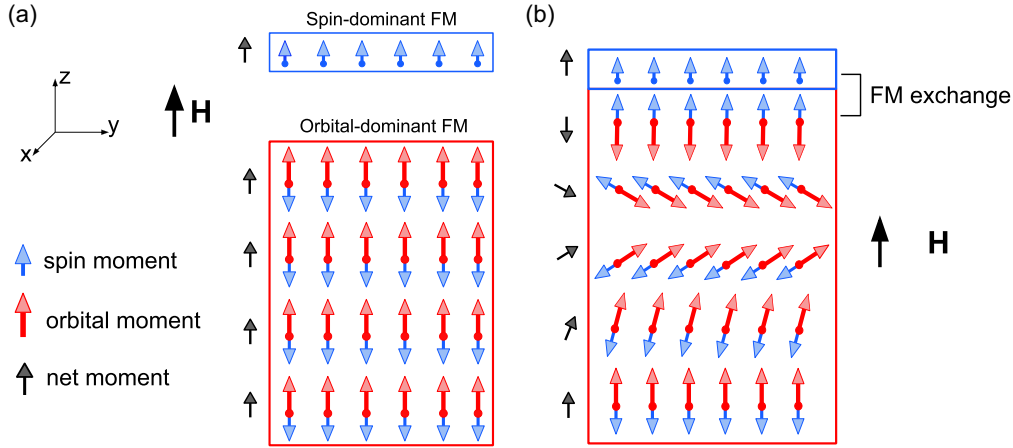


FIG. 1. (Color online) (a) A sketch of a single atomic layer of a spin-dominant ferromagnet (e.g., GdN) and a cross section of multiple planes of an orbital-dominant (SmN) ferromagnet. (b) Cross section of an interface between spin- and orbital-dominant ferromagnets. A twisted phase develops in the orbital-dominant ferromagnet due to exchange-Zeeman competition, which occurs if the spin-dominant layer remains fixed due to its large Zeeman coupling.

It is important to note that the GdN/SmN system is fundamentally different from the conventional spin-dominant ferromagnetic systems displaying twisted phases. The most common exchange spring systems, composed of hard and soft ferromagnetic layers, are first magnetized in one direction, and when the field is reversed the hard material remains fixed while an exchange spiral is formed in the soft material [8,26]. In another manifestation, metallic Gd/Fe systems displaying twisted phases rely on antiferromagnetic coupling between spins at the interface [7,27–31]. With the SmN/GdN system, however, the interlayer Sm-Gd exchange is ferromagnetic, and the usual hard/soft contrast is of no interest; indeed, the fixed layer (GdN) has a coercive field three orders of magnitude smaller than SmN. It is the much stronger Zeeman interaction in GdN than in SmN that effectively locks the GdN magnetization. Furthermore, the spin-dominant metallic systems lack the novel combination of electronic and magnetic properties of SmN and GdN, which allow the facility of controlling the concentration and sign of charge carriers without disturbing the ferromagnetic ordered state, and band-structure results also show electron and hole channels of majority spin [32].

In our investigation of the interface exchange coupling in GdN/SmN multilayers, we have used the element selectivity of x-ray magnetic circular dichroism (XMCD) at the Sm $L_{2,3}$ and $M_{4,5}$ edges. We first demonstrate that the SmN is ferromagnetically exchange-coupled to GdN through investigation of a SmN/GdN superlattice. We then demonstrate that a twisted, or rotating, magnetization develops in ultrathin SmN films coupled to GdN due to interface pinning in the SmN, short-range interionic rare-earth exchange, and the extremely weak Zeeman coupling of SmN. The observed depth dependence of the magnetization is fully consistent with an analytical model based on these competing interactions.

II. EXPERIMENTAL DETAILS

The attenuation lengths of hard L -edge and soft M -edge x rays dictated that quite different structures were used for

the two investigations. At the L edge, the full thickness of a superlattice of $12 \times (1.5 \text{ nm SmN}/9 \text{ nm GdN})$ was probed through a 100 nm passivating AlN cap. For the much more surface-sensitive M edge, we investigated two samples. The first was a bilayer of 100 nm GdN/ 5.5 nm SmN, and the second, a trilayer of 100 nm GdN/ 6 nm LaN/ 5.5 nm SmN. The nonmagnetic LaN layer between the GdN and SmN was included to block the Gd-Sm exchange interaction in the trilayer. Both of the M -edge samples were passivated with 25 nm of GaN to prevent sample oxidation.

Samples were grown in a thermionics ultrahigh-vacuum system with a base pressure of 1×10^{-8} Torr. High-purity Gd metal was evaporated at a rate of 0.2 \AA/s with an N_2 partial pressure of 4.5×10^{-4} Torr. Sm metal was evaporated at a rate of 0.3 \AA/s under the same N_2 pressure. The superlattice was grown on an MgO(111) substrate, while the bi- and trilayers were grown on c -plane Al_2O_3 substrates. All the substrates were outgassed for 1 h at $700 \text{ }^\circ\text{C}$, and heated to $600 \text{ }^\circ\text{C}$ during growth. The GaN and AlN capping layers were grown at room temperature with the metal evaporated at a rate of 0.1 \AA/s with an ion source activating the N_2 . Thicknesses were determined via quartz crystal balances calibrated for SmN, GdN, AlN, and GaN via scanning electron microscope and Rutherford backscattering measurements. The SmN/GdN superlattice was characterized *ex situ* by XRD, and it showed the lattice constant of GdN; as expected, the in-plane lattice constant was dominated by the thicker GdN layers in all cases.

Magnetization measurements were carried out via a Quantum Design SQUID with the field oriented in-plane. Because the much larger magnetic moment of GdN drowns out the signal from SmN, SQUID measurements probe only the GdN magnetization. Curie-Weiss fits to the inverse susceptibility yielded paramagnetic Curie temperatures of 69, 68, and 66 K for the superlattice, trilayer, and bilayer, respectively. Hysteresis loops measured at 5 K saturated at $7\mu_B$ per Gd^{3+} ion. The superlattice and bilayer displayed a coercive field of 120 Oe at 5 K, while the trilayer had a coercive field of 90 Oe, all within the range reported for polycrystalline GdN films [23,33].

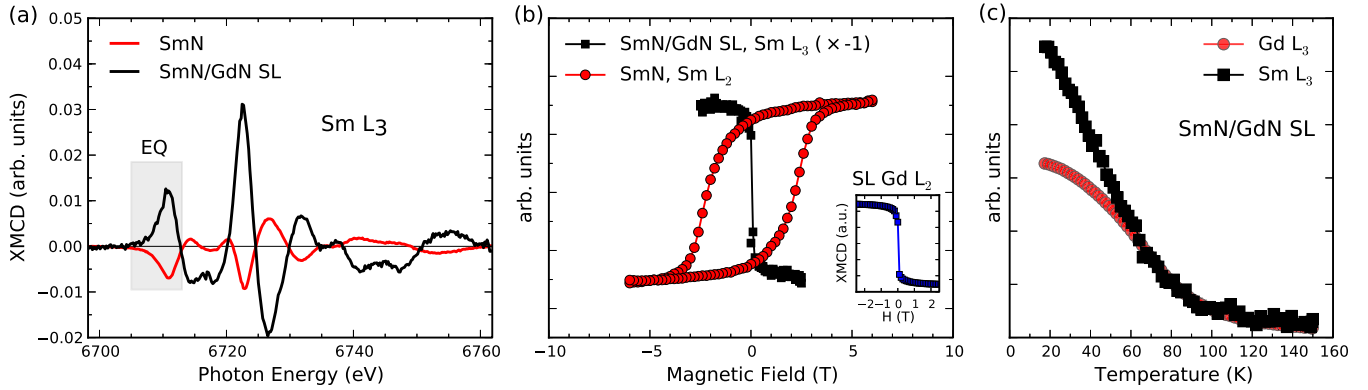


FIG. 2. (Color online) (a) XMCD at the $\text{Sm } L_3$ edge in a SmN/GdN superlattice (black) and a homogeneous SmN film (red) taken at 15 K, and in grazing incidence. The signal above 6715 eV is predominantly due to electric dipole transitions into the $5d$ shell, and below that the signal is due to electric quadrupole transitions (EQ) into the empty $4f$ orbitals. (b) XMCD-derived hysteresis taken at 15 K and measured at the $\text{Sm } L_2$ edge for the superlattice (squares) and at the $\text{Sm } L_3$ edge for the bulk SmN film (circles). The superlattice spectra were scaled by -1 . The inset shows the Gd L_2 edge hysteresis taken at 15 K. (c) Temperature dependence of Gd L_3 and Sm L_3 peaks in a field of 2.5 T for the SmN/GdN superlattice.

XMCD measurements were performed at temperatures down to 15 K and fields up to 6 T at the Sm and Gd $L_{2,3}$ edges on beamline ID12 at the European Synchrotron Radiation Facility (ESRF) in Grenoble. $M_{4,5}$ -edge XMCD was measured at the soft-x-ray line ID08 of the ESRF, at temperatures to 10 K and in fields up to 4 T. Measurements at the M edge were necessarily performed only at normal incidence to limit attenuation by a passivating cap. For all of the L -edge XMCD measurements, the field and incident beam were directed at 10° from grazing incidence, in which geometry the very large shape anisotropy ($4\pi\mathcal{M} \sim 2$ T, where \mathcal{M} is the magnetization) of GdN ensured that the magnetization lay in the plane of the film. At both edges, the applied magnetic field was along the x-ray propagation direction.

The XMCD spectra were obtained by taking the difference of two XAS spectra with the x-ray helicity reversed while the magnetic field was held fixed. This corresponds to the difference between antiparallel and parallel alignments of the helicity and magnetization. XAS spectra have been normalized to the incident photon intensity. XMCD spectra were normalized to the XAS white line intensity at the M edge and to the edge jump at the L edge. XAS and XMCD spectra for Sm and Gd L edges appear in the supplemental material [34] (Fig. S1), along with Sm and Gd $M_{4,5}$ -edge XAS (Figs. S2 and S3).

XMCD at the $\text{Sm } L_2$ edge is the signal of choice for following magnetic hysteresis, for it is stronger than the L_3 -edge signal. In the superlattice, that feature was obscured by magnetic EXAFS (extended x-ray absorption fine structure) from the Gd L_3 edge, necessitating the use of the $\text{Sm } L_3$ XMCD in the superlattice. There was a similar interference in the soft-x-ray measurements, where the capping-layer Ga $L_{2,3}$ edge introduced a large and variable background in the Gd $M_{4,5}$ -edge XAS.

Our investigation relies on the use of two common schemes for measuring the x-ray absorption and XMCD spectra, based on the emission of fluorescence [total fluorescence yield (TFY)] or electrons (TEY). Below, we exploit the differing probing depths of these two schemes in our soft-x-ray $M_{4,5}$

edges, where TFY probes the full 5.5 nm of the SmN layers while TEY data probe a depth of ~ 2 nm. Saturation effects distorted the TFY mode at the $\text{Sm } M_{4,5}$ edges, but nonetheless provide relative comparisons between different samples.

III. L -EDGE XMCD RESULTS

We first discuss the hard-x-ray results; Fig. 2(a) shows XMCD data from the superlattice at the $\text{Sm } L_3$ edge, compared to the $\text{Sm } L_3$ in homogeneous SmN. The XMCD spectra from these samples are taken from Ref. [25] (see also the supplemental material [34]). These spectra primarily show the dipole transitions from $2p$ to empty $5d$ orbitals, with weaker quadrupolar excitations to the $4f$ shell, and thus signal the strength and sign of the spin and orbital alignments of the $5d$, and less quantifiably, the $4f$ shells. The $5d$ states participate in the ordering through $4f$ - $5d$ exchange, though the exchange mechanism between $5d$ states is not well understood [35]. The XMCD sign reversal shown in Fig. 2(a) between homogeneous SmN and thin SmN layers embedded in GdN immediately indicates that Sm-Gd interface exchange determines the Sm spin alignment, dominating the weak Zeeman interaction that aligns the net, orbital-dominated, moment in homogeneous SmN.

The hysteresis displayed in Fig. 2(b) compares the hysteresis between homogeneous SmN and SmN in the superlattice, further demonstrating that the SmN coercive field in the superlattice is reduced to ~ 0.01 T, emphasizing that the SmN magnetization is firmly coupled to the GdN by the exchange interaction across the GdN/SmN interfaces. We note that the hysteresis in the homogeneous SmN film was measured using the L_2 edge, the signal of choice for its substantially larger XMCD signal, but the masking of that signal by Gd magnetic EXAFS (extended x-ray absorption fine structure) dictated the use of the weaker L_3 edge in the superlattice. There is an intrinsic sign difference between the most prominent XMCD features at the $\text{Sm } L_2$ and L_3 edges [25], so we have scaled the L_3 -derived hysteresis by -1 in Fig. 2(b) in order to indicate the antiparallel spin/orbit alignment between samples, which is clear from the direct L_3 -edge comparison in Fig. 2(a).

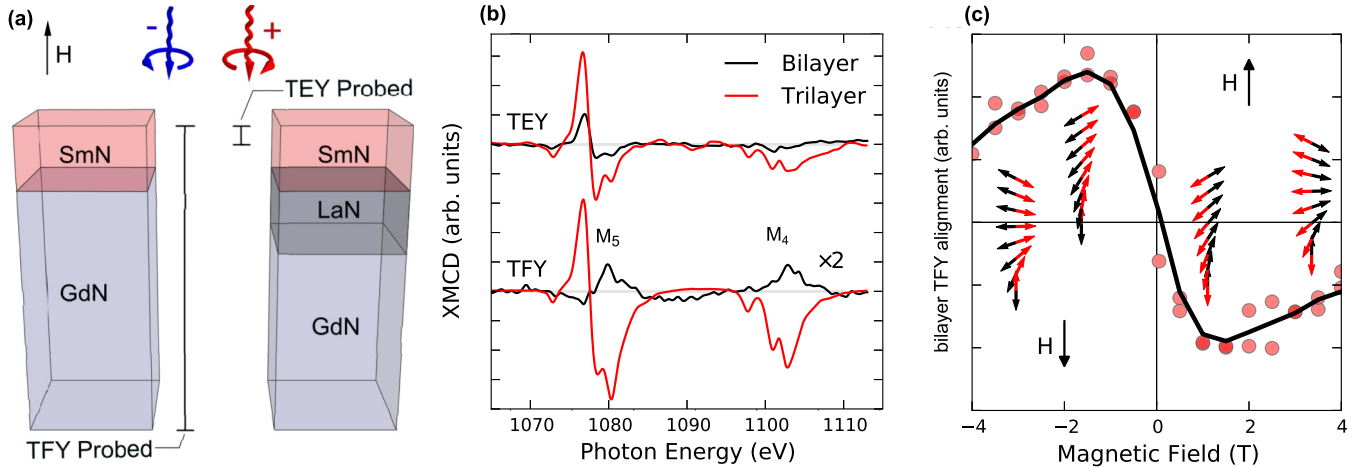


FIG. 3. (Color online) (a) Bilayer and trilayer field-normal XMCD geometry at the $M_{4,5}$ edge, with the approximate probing depths of the XMCD signal in the TEY and TFY detection modes sketched. (b) The $M_{4,5}$ -edge XMCD spectra for the bilayer (black) and trilayer (red) taken at $H = 4$ T and 10 K. The bilayer TFY signal has been scaled by 2 for visibility. (c) The bilayer hysteresis derived from the Sm M-edge XMCD in the TFY mode, with the field normal geometry. The shaded circles show data points while the black line, which represents a smoothed average, is a guide to the eye. The arrows represent the spin moment (black arrows) and orbital moment (red arrows) through the SmN in the bilayer.

The temperature dependencies of the GdN L_3 and SmN L_3 XMCD from the superlattice are compared in Fig. 2(c), showing Sm alignment following Gd well above the 27 K SmN Curie temperature. Clearly the Sm moments in interface-adjacent ions are again aligned across the interface. At lower temperatures, the Sm moment continues to rise faster than does the rapidly saturating GdN, as the Sm ions deeper in the SmN layer align by the Sm-Sm exchange interaction.

IV. M-EDGE XMCD RESULTS

We access the magnetic alignment of SmN more directly by turning to the soft-x-ray $M_{4,5}$ edges, which represent $3d \rightarrow 4f$ transitions and thus signal the spin and orbital alignment in the $4f$ shell. Figure 3(a) sketches the geometry of the M -edge measurements, with the magnetic field and x rays parallel to the surface normal.

Figure 3(b) shows the Sm $M_{4,5}$ edges XMCD in both TEY and TFY modes for the two samples (see the supplemental material [34] for XAS spectra). For the trilayer, the TFY and TEY spectra in the SmN layer are in excellent agreement, establishing common SmN $4f$ alignment in the near-surface region (TEY) and the bulk (TFY); clearly the SmN is effectively decoupled from GdN by the LaN blocking layer. In contrast, both TFY and TEY signals are substantially weaker in the bilayer, and the TFY signal is even inverted. The latter is a signature of SmN that is strongly coupled to the GdN by exchange across the GdN/SmN interface.

To quantify the differences in XMCD between samples, we have fit the Sm $M_{4,5}$ spectra in the bilayer to that in the uniformly aligned trilayer. The procedure is justified by the strong spin-orbit coupling of the $4f$ electrons, which keeps spin and orbital moments firmly aligned relative to each other [36,37]. The XMCD sum rules [38,39] then imply that the XMCD spectral shape should remain the same between the samples, with a scaling factor as a measure of the depth-averaged (TFY) and near-surface (TEY) alignment.

Fitting of the spectra yields spin/orbital-alignment ratios of bilayer-to-trilayer of $R_{\text{TEY}} = 0.20 \pm 0.07$ and $R_{\text{TFY}} = -0.12 \pm 0.02$. For the bilayer, therefore, the alignment in the surface ~ 2 nm probed by TEY is Zeeman-dominated, though its alignment with the field is only 20% of that in bulk SmN. In contrast, the average through the film is of opposite sign, determined by exchange across the GdN/SmN interface, as was found also in the very thin SmN layers in the superlattice in the $L_{2,3}$ -edge study mentioned above. Clearly there is an inhomogeneous alignment in the bilayer, i.e., a rotation of the spin and orbital moments as sketched in Fig. 4(a).

Figure 3(c) shows an unusual hysteresis curve extracted from the bulk sensitive TFY measurement of the bilayer, where SmN is deposited directly on GdN. The same fitting procedure mentioned above was used to extract the hysteresis. The Sm $4f$ alignment in this case shows the same sign inversion seen in the $L_{2,3}$ -edge data in Fig. 2(b), but with diminishing alignment with increasing fields larger than ~ 1.5 T. It is important to notice that in the field-normal configuration, the shape anisotropy of GdN prevents a saturated magnetization in applied fields smaller than ~ 2 T. Its magnetization rises approximately linearly with weaker applied fields, but for larger fields the GdN is saturated; between 2 and 4 T, the $4f$ spins are fully aligned and exert the full Gd-Sm exchange on the SmN $4f$ spin moment at the interface. In this region, the increasing field has the effect of modifying the exchange-Zeeman competition, which in turn reduces the bulk averaged XMCD signal as the $4f$ spin and orbital moments rotate through the film. In the following section, we pursue deeper insight into the nature of the twisting, or rotating magnetization.

V. ANALYSIS AND DISCUSSION

In this section, we relate the measured TEY and TFY XMCD results in the bilayer to a model of the twisting SmN magnetization. We consider a one-dimensional model of the

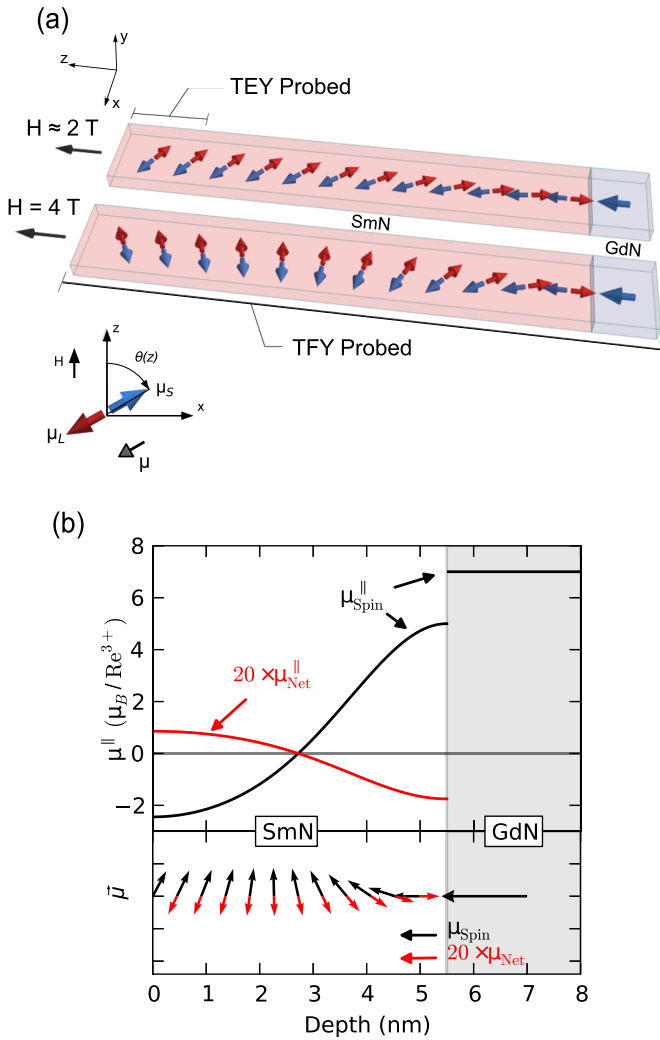


FIG. 4. (Color online) (a) A sketch of the in-plane twisted magnetization structure near the SmN-GdN interface with spin moments (blue) and orbital moments (red). (b) Calculation of the spin and net moment as a function of depth in the SmN layer of the bilayer. The Gd moment is fixed at $7\mu_B$ through the GdN film, and the Sm spin moment is pinned at the SmN/GdN interface to its maximum value of $5\mu_B$.

SmN magnetization in the bilayer, in which the resulting magnetization profile is determined by the balance among (i) the Sm-Sm exchange energy acting on Sm spin moments, (ii) the Zeeman energy acting on the SmN net moment, and (iii) the demagnetization field of SmN. We note that the shape anisotropy for SmN is only 0.01 T; under the large fields of interest here, the demagnetization field responsible for the shape anisotropy can be neglected in comparison to the Zeeman energy. While anisotropy should play some role, there are no studies of its effects in SmN [24], and our results suggest it is only a weak correction. Treating the exchange as acting between atomic planes parallel to the interface, the total energy per unit area in a continuum approximation [6,8] is then

$$\mathcal{E} = \int_0^d dz \left[A \left(\frac{d\theta(z)}{dz} \right)^2 - \mathbf{M}_S \cdot \mathbf{H} \right], \quad (1)$$

where A is the exchange stiffness, \mathbf{M}_S is the saturation magnetization of the SmN, $\mathbf{H} = H\hat{z}$ is the applied field, and $d = 5.5$ nm is the thickness of the SmN film. $\theta(z)$ is the depth-varying angle between \mathbf{H} and the spin moment μ_S [see Fig. 4(a)]. The Zeeman term adopts the opposite sign as found in conventional spin-dominant systems because the net moment is antiparallel to the μ_S , hence $-\mathbf{M}_S \cdot \mathbf{H} = M_S H \cos \theta(z)$. The exchange stiffness A is estimated from the experimental Curie temperature of SmN using the mean-field approximation [40].

Equation (1) can be minimized analytically to yield the most energetically favorable configuration, as carried out by Goto *et al.* [8] for an exchange-spring system, yielding an expression for $\theta(z)$ in terms of Jacobi elliptic functions (see the supplemental material [34] for details). The boundary conditions were chosen such that $\theta(d) = 0$ (Sm spin is aligned with the Gd spin at the SmN-GdN interface) and $d\theta(z)/dz|_{z=0} = 0$ (SmN free surface). These boundary conditions account for the magnetically soft GdN being rigidly fixed parallel to the applied field due its large Zeeman interaction. This fixed GdN then acts as the rigid pinning layer for the SmN at the interface. We emphasize that this is in strong contrast to conventional spin-dominant exchange-spring systems, where the pinning layer must have a large coercive field in order to remain rigid because the field is applied *antiparallel* to its magnetization.

Within the model, a twisted phase develops on a scale of $\ell = \pi/2\sqrt{2A/HM_S}$; below this thickness, a uniform magnetization [$\theta(z) \equiv 0$] is favored for given parameters. In an applied field of 4 T, this corresponds to $\ell \approx 4$ nm, on the order of the SmN film thickness. Figure 4(b) shows the calculation of the net moment and spin moment projected on the z axis [i.e., $\mu \cos \theta(z)$ and $\mu_S \cos \theta(z)$], as a function of the depth z in the 4 T field. The length scale of the twist increases in a field of 2 T as the Zeeman energy weakens, illustrated in Fig. 4(a) and the inset of Fig. 3(c).

The resulting depth profile of the net SmN moment projected along the z axis, $\mu \cos \theta(z)$, can be compared to the XMCD spectra by accounting for the depth-averaging of the XMCD measurement, in combination with the effective sampling depth in the TXY (TEY or TFY) measurement schemes, λ_{TXY} . The finite sampling depth λ_{TXY} in the TXY mode results in a detection efficiency $w_{\text{TXY}} = e^{-z/\lambda_{\text{TXY}}}$ from a depth z [41]. Thus we can approximate the depth-averaged XMCD measurement as returning an effective net moment of

$$\langle \mu \rangle_{\text{TXY}} = \frac{1}{d} \int_0^d dz \mu \cos \theta(z) e^{-z/\lambda_{\text{TXY}}}. \quad (2)$$

Absolute values of μ_S and the orbital moment μ_L can in principle be extracted by applying the XMCD sum rules, however they require much greater signal-to-noise ratios than are available with the present data. Instead, we note that μ_S and μ_L in both samples are fixed antiparallel by the strong spin-orbit coupling, and the energy dependence of the XMCD spectra remains unchanged. The ratios of $\langle \mu \rangle_{\text{TXY}}$ between the bilayer and trilayer are thus expressions for the experimentally determined ratios, which simply reflects the depth average of $\cos \theta(z)$ within the bilayer. The calculated ratio $R_{\text{TXY}} = \langle \mu \rangle_{\text{TXY}}^{\text{bilayer}} / \langle \mu \rangle_{\text{TXY}}^{\text{trilayer}}$ in the TFY mode gives $R_{\text{TFY}} = -0.11$, in excellent agreement with the measured ratio of -0.12 ± 0.02 .

R_{TFY} is insensitive to precise value of λ_{TXY} (≈ 100 nm), as $d \ll \lambda_{\text{TFY}}$; the fluorescence is effectively unattenuated. The TEY-channel ratio depends more strongly on λ_{TEY} ; the experimental value of $R_{\text{TEY}} = 0.20$ is returned for an electron escape depth of $\lambda_{\text{TEY}} = 2.15$ nm, which is consistent with the expected range [41,42]. The excellent agreement of this analytical model with the experimentally measured spectra thus strongly supports the mechanism of exchange-Zeeman competition driving the twisted magnetization in the SmN layer coupled to GdN.

The agreement achieved by using only experimental parameters and reasonable values of λ_{TXY} is encouraging and indicates that other effects, including bulk and surface anisotropies, are only weak corrections to the exchange- and Zeeman-dominated contributions. We add that the continuum approximation leading to Eq. (1) has been shown to be in good agreement with more exact treatments using a discretized version of the model, even down to a few monolayers [43].

VI. CONCLUSION

In summary, we have observed a twisted magnetization phase in a SmN/GdN bilayer by exploiting the depth dependence of the electron-yield and fluorescence-yield detection modes at the rare-earth M -edge XMCD. The interfacial pinning of the SmN moment to GdN was clearly demonstrated in the L -edge XMCD measurements, showing that the

ferromagnetic GdN-SmN exchange coupling is responsible for the pinning. The decoupling of the SmN and GdN magnetization in the SmN/LaN/GdN structure points toward magnetic tunnel junctions, especially attractive within the RENs due to their epitaxial compatibility across the series. The appearance of a twisted phase in the SmN/GdN system also holds intriguing possibilities for spintronics applications, due to the semiconducting nature of the pair coupled with the orbital-dominant magnetism of SmN. For example, the tuning of the twisted phase length scale $\ell \sim \sqrt{A/HM_S}$ for given fields can be achieved through doping, or replacement, with other rare-earth elements, thus modifying the exchange A and the saturation magnetization M_S [44]. The ability to control the scale of what is effectively a domain-wall width in intrinsic ferromagnetic semiconductor heterostructures also allows for the opportunity to explore spin-orbit torques across controllable domain-wall widths.

ACKNOWLEDGMENTS

We acknowledge financial support from the New Zealand Foundation for Research, Science and Technology (Grant No. VICX0808) and the Marsden Fund (Grant No. 08-VUW-030). The MacDiarmid Institute is supported by the New Zealand Centres of Research Excellence Fund. E.A. thanks the Alexander-von-Humboldt Foundation for support through a fellowship.

-
- [1] S. S. Parkin, M. Hayashi, and L. Thomas, *Science* **320**, 190 (2008).
 - [2] A. Thiaville, S. Rohart, É. Jué, V. Cros, and A. Fert, *Europhys. Lett.* **100**, 57002 (2012).
 - [3] S. Emori, U. Bauer, S.-M. Ahn, E. Martinez, and G. S. Beach, *Nat. Mater.* **12**, 611 (2013).
 - [4] A. V. Khvalkovskiy, V. Cros, D. Apalkov, V. Nikitin, M. Krounbi, K. A. Zvezdin, A. Anane, J. Grollier, and A. Fert, *Phys. Rev. B* **87**, 020402 (2013).
 - [5] H. Zocher, *Trans. Faraday Soc.* **29**, 945 (1933).
 - [6] A. Thiaville and A. Fert, *J. Magn. Magn. Mater.* **113**, 161 (1992).
 - [7] R. E. Camley, *Phys. Rev. B* **35**, 3608 (1987).
 - [8] E. Goto, N. Hayashi, T. Miyashita, and K. Nakagawa, *J. Appl. Phys.* **36**, 2951 (1965).
 - [9] A. Berkowitz and K. Takano, *J. Magn. Magn. Mater.* **200**, 552 (1999).
 - [10] A. N. Bogdanov and U. K. Röbber, *Phys. Rev. B* **68**, 012407 (2003).
 - [11] A. N. Bogdanov and U. K. Röbber, *Phys. Rev. Lett.* **87**, 037203 (2001).
 - [12] U. K. Röbber, A. N. Bogdanov, and C. Pfeleiderer, *Nature (London)* **442**, 797 (2006).
 - [13] F. Natali, B. J. Ruck, N. O. V. Plank, H. J. Trodahl, S. Granville, C. Meyer, and W. R. L. Lambrecht, *Prog. Mater. Sci.* **58**, 1316 (2013).
 - [14] F. Leuenberger, A. Parge, W. Felsch, K. Fauth, and M. Hessler, *Phys. Rev. B* **72**, 014427 (2005).
 - [15] S. Granville, B. J. Ruck, F. Budde, A. Koo, D. J. Pringle, F. Kuchler, A. R. H. Preston, D. H. Housden, N. Lund, A. Bittar, G. V. M. Williams, and H. J. Trodahl, *Phys. Rev. B* **73**, 235335 (2006).
 - [16] A. R. H. Preston, S. Granville, D. H. Housden, B. Ludbrook, B. J. Ruck, H. J. Trodahl, A. Bittar, G. V. M. Williams, J. E. Downes, A. DeMasi, Y. Zhang, K. E. Smith, and W. R. L. Lambrecht, *Phys. Rev. B* **76**, 245120 (2007).
 - [17] C. Meyer, B. J. Ruck, A. R. H. Preston, S. Granville, G. V. M. Williams, and H. J. Trodahl, *J. Magn. Magn. Mater.* **322**, 1973 (2010).
 - [18] M. Azeem, B. J. Ruck, B. Do Le, H. Warring, H. J. Trodahl, N. M. Strickland, A. Koo, V. Goian, and S. Kamba, *J. Appl. Phys.* **113**, 203509 (2013).
 - [19] D. Le Binh, B. J. Ruck, F. Natali, H. Warring, H. J. Trodahl, E.-M. Anton, C. Meyer, L. Ranno, F. Wilhelm, and A. Rogalev, *Phys. Rev. Lett.* **111**, 167206 (2013).
 - [20] K. Senapati, M. G. Blamire, and Z. H. Barber, *Nat. Mater.* **10**, 849 (2011).
 - [21] P. K. Muduli, A. Pal, and M. G. Blamire, *Phys. Rev. B* **89**, 094414 (2014).
 - [22] F. Natali, B. J. Ruck, H. J. Trodahl, D. L. Binh, S. Veizan, B. Damilano, Y. Cordier, F. Semond, and C. Meyer, *Phys. Rev. B* **87**, 035202 (2013).
 - [23] B. M. Ludbrook, I. L. Farrell, M. Kuebel, B. J. Ruck, A. R. H. Preston, H. J. Trodahl, L. Ranno, R. J. Reeves, and S. M. Durbin, *J. Appl. Phys.* **106**, 063910 (2009).
 - [24] C. Meyer, B. J. Ruck, J. Zhong, S. Granville, A. R. H. Preston, G. V. M. Williams, and H. J. Trodahl, *Phys. Rev. B* **78**, 174406 (2008).
 - [25] E.-M. Anton, B. J. Ruck, C. Meyer, F. Natali, H. Warring, F. Wilhelm, A. Rogalev, V. N. Antonov, and H. J. Trodahl, *Phys. Rev. B* **87**, 134414 (2013).
 - [26] E. E. Fullerton, J. S. Jiang, M. Grimsditch, C. H. Sowers, and S. D. Bader, *Phys. Rev. B* **58**, 12193 (1998).

- [27] R. E. Camley and D. R. Tilley, *Phys. Rev. B* **37**, 3413 (1988).
- [28] C. Dufour, K. Cherifi, G. Marchal, P. Mangin, and M. Hennion, *Phys. Rev. B* **47**, 14572 (1993).
- [29] W. Hahn, M. Loewenhaupt, Y. Y. Huang, G. P. Felcher, and S. S. P. Parkin, *Phys. Rev. B* **52**, 16041 (1995).
- [30] E. Kravtsov, D. Haskel, S. G. E. te Velthuis, J. S. Jiang, and B. J. Kirby, *Phys. Rev. B* **79**, 134438 (2009).
- [31] A. Koizumi, M. Takagaki, M. Suzuki, N. Kawamura, and N. Sakai, *Phys. Rev. B* **61**, R14909 (2000).
- [32] P. Larson, W. R. L. Lambrecht, A. Chantis, and M. van Schilfgaarde, *Phys. Rev. B* **75**, 045114 (2007).
- [33] F. Natali, N. O. V. Plank, J. Galipaud, B. J. Ruck, H. J. Trodahl, F. Semond, S. Sorieul, and L. Hirsch, *J. Cryst. Growth* **312**, 3583 (2010).
- [34] See Supplemental Material at <http://link.aps.org/supplemental/10.1103/PhysRevB.91.174426> for the XAS and XMCD spectra for Sm and Gd *L* edges, and for details of the twisted phase model.
- [35] C.-G. Duan, R. F. Sabirianov, W. N. Mei, P. A. Dowben, S. S. Jaswal, and E. Y. Tsybal, *J. Phys.: Condens. Matter* **19**, 315220 (2007).
- [36] G. van der Laan and B. T. Thole, *Phys. Rev. B* **53**, 14458 (1996).
- [37] S. S. Dhesi, G. van der Laan, P. Bencok, N. B. Brookes, R. M. Galéra, and P. Ohresser, *Phys. Rev. B* **82**, 180402 (2010).
- [38] B. T. Thole, P. Carra, F. Sette, and G. van der Laan, *Phys. Rev. Lett.* **68**, 1943 (1992).
- [39] P. Carra, B. T. Thole, M. Altarelli, and X. Wang, *Phys. Rev. Lett.* **70**, 694 (1993).
- [40] J. B. Goodenough *et al.*, *Magnetism and the Chemical Bond* (Interscience, New York, 1963), Vol. 98.
- [41] J. Stöhr and H. C. Siegmann, *Magnetism: From Fundamentals to Nanoscale Dynamics* (Springer, Berlin, 2006), Vol. 152.
- [42] B. T. Thole, G. van der Laan, J. C. Fuggle, G. A. Sawatzky, R. C. Karnatak, and J.-M. Esteve, *Phys. Rev. B* **32**, 5107 (1985).
- [43] G. Bowden, J. Beaujour, S. Gordeev, P. de Groot, B. Rainford, and M. Sawicki, *J. Phys.: Condens. Matter* **12**, 9335 (2000).
- [44] H. Adachi and H. Ino, *Nature (London)* **401**, 148 (1999).